

© 2015 IEEE. Personal use of this material is permitted. Permission from IEEE must be obtained for all other uses, in any current or future media, including reprinting/republishing this material for advertising or promotional purposes, creating new collective works, for resale or redistribution to servers or lists, or reuse of any copyrighted component of this work in other works.

This paper has been accepted for publication by

**IEEE Transactions on Power Electronics.**

**DOI**

10.1109/TPEL.2015.2441005

**Citation**

W. Liang, L. Raymond and J. Rivas, "3-D-Printed Air-Core Inductors for High-Frequency Power Converters," *IEEE Trans. Power Electronics*, vol. 31, no. 1, pp. 52-64, Jan. 2016.

**IEEE Xplore URL**

<http://ieeexplore.ieee.org/document/7116563>

More papers from Juan Rivas's group at Stanford University can be found here:

<http://superlab.stanford.edu/publications.html>

# 3D Printed Air Core Inductors for High Frequency Power Converters

Wei Liang, *Student Member, IEEE*, Luke Raymond, *Student Member, IEEE*, and Juan Rivas, *Member, IEEE*

**Abstract**—This paper presents the design, modeling and characterization of 3D printed air core inductors for high frequency power electronics circuits. The use of 3D modeling techniques to make passive components extends the design flexibility and addresses some of the fabrication limitations of traditional processes. Recent work [1]–[9] has demonstrated the feasibility of incorporating air core inductors in high frequency ( $>10$  MHz) switching power converters. These implementations have used discrete wire wound solenoids and toroids, and planar components that use Printed Circuit Board (PCB) traces or microfabrication techniques to make air core inductors. However, realizations of such components have limitations in performance and applicability including open paths conducive to the flow of leakage fields, and difficulties in achieving optimal cross-section to minimize loss. Along with the current effort of involving 3D printing technology to make inductors [10], [11], we propose the use of 3D printing and casting/plating techniques as a simple and accessible alternative that adds flexibility and functionality to air core inductor design for high frequency power conversion at moderate to high power (e.g. tens to thousands of watts) and high voltage (greater than 100 V) levels. In this paper, we present several examples of air core inductors realized using 3D printing and casting/plating techniques to give an idea of the geometries that are possible to design. Moreover, we show that some of these designs can lead to improved electrical performance.

The paper also describes the tools used by the authors to design, fabricate and characterize the electromagnetic performance of the air core inductors. The software used to generate the 3D scaffolds for the inductors are freely available and easily accessible. Readers are encouraged to explore more possibilities of geometries that can lead to better performance with the ease of manufacturing. As progress in additive manufacturing continues, we envision 3D printing of a complete scaffold structure that after plating (or casting) will contain all resonant passive components of an RF switching converter. Toward this goal, we present a 70 W prototype 27.12 MHz resonant inverter that incorporates some of the 3D printed components developed for this work.

**Index Terms**—3D printed air core inductor, high frequency power converters.

## I. INTRODUCTION

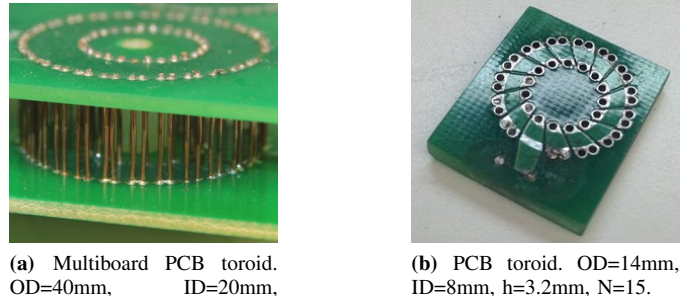
Air core inductors are simple devices that can be realized in multiple ways, depending on the circuit requirements and fabrication constraints.

Previous implementations include wire wound solenoids and toroids. These inductor implementations are simple and provide some tuning flexibility, but have limitations: They have low copper utilization due to skin effect at the switching frequency of 10s of MHz, which forces the current to flow on the

The authors are with Stanford University, Stanford, CA, 94305 (e-mail:liangw@stanford.edu, lraymond@stanford.edu, jmriivas@stanford.edu).

This work has been presented at 2014 IEEE Energy Conversion Congress and Exposition (ECCE), Pittsburgh, PA, 2014.

very inner sheet of conductor, leaving the bulk of the copper un-utilized. Also, to avoid interaction with nearby components, the effective volume allotted to the solenoid should include the full volume of the magnetic field. This volume can extend well beyond the physical volume of the inductor itself. Wire wound toroids constrain the bulk magnetic flux to the torus thus reducing coupling to other components. However, the constant diameter conductor provides poor copper coverage at the outer diameter causing magnetic flux leakage. Work in [12], [13] has shown improvements to toroidal implementations. The authors used folded foil and milling techniques to improve copper coverage and performance of air core toroids for high frequency converters.



(a) Multiboard PCB toroid.  
OD=40mm, ID=20mm,  
h=9.56mm, N=28.

(b) PCB toroid. OD=14mm,  
ID=8mm, h=3.2mm, N=15.

**Fig. 1:** PCB toroid inductors in [2] and [3]. In Fig. 1a, the top and bottom of the toroid are printed on two separated PCBs. Copper wires are used to complete the vertical connections. In Fig. 1b, the toroid is printed directly on a 3.2mm thickness PCB.

PCBs have been used to make air core inductors [2], [3], [14]–[19] with various shapes including spirals [14]–[16], [19], solenoids [18] and toroids [2], [3], [17]. Since toroidal inductors have relatively low external magnetic fields, they are favored in many applications where it is important to mitigate unintentional coupling and reduce eddy current losses. Work in [17] demonstrates various single PCB board toroid inductors. These are easy to fabricate and have low part to part variation. Moreover, as mentioned in [2], automatic design scripts to generate the layout can greatly reduce the time involved in iterative design processes.

However, [13] and references within, explain that under height and specific dimensional constraints, the inductor cross section that maximizes inductor  $Q$  is not rectangular. The limited number of conductive layers and limitations in the number of vias that can be economically achieved in common single PCB manufacturing means that achievable toroidal cross sections are suboptimal for larger inductors (e.g. hundreds of

nH) with high quality factors (e.g. more than 100 at 27.12 MHz). Thus, the multiboard PCB toroid used in [2] of Fig. 1a was designed to maintain a cross section aspect ratio closer to optimum at the expense of fabrication complexity. However, the large number of solder points used in the process (and visible in Fig. 1a) increases current path resistance and makes the implementation difficult.

These PCB toroidal implementations improve copper coverage of the top and bottom sides of the magnetic structure, but leave the vertical sides porous. The limited number of vias that can be located at the inner and outer edges of the structure invariably result in leaking flux on the sides of the structure. Work in [20], [21] proposed a hybrid inductor concept that combines copper foil [22] and PCB to form a solid vertical connection. This approach successfully mitigates stray fields but adds complexity to the implementation process. Other PCB fabrication methods including the use of micro-vias and/or castellations can reduce the porosity of the sides as well but often at great expense.

Microfabrication technologies have also been investigated to fabricate air core inductors directly on IC chips for Power System on Chip (PSoC) applications [4]–[9], [23], [24]. While state of art microfabrication processes can produce complex and intricate shapes using various creative methods [25]–[30], this process lends itself to inductor designs ideal for relatively low power systems. Such techniques are often not well suited for power electronics applications with moderate to high power levels (e.g. tens to thousands of watts) and high operating voltages (e.g.  $> 100$  V). In addition, high cost equipments and a contamination free environment are necessary for prototyping and production.

Another leading fabrication technique capable of realizing very complicated circuits and components is called Nuvotonics Polystrata [31]–[36]. This sophisticated process is generally used for circuits operating in the 10s and 100s of GHz. As an example, the inductor shown in [35], a 2 mm long solenoid design with vertical walls, is a potential application for this particular process. However, no examples of designs with cross-sections having curved or rounded features in the vertical direction were found in the literature.

Along with the current effort of involving 3D printing technology to make inductors [10], [11], we propose the use of 3D printing and plating/casting techniques to design air core inductors for high frequency power converter operating at tens to thousands of watts and hundreds of volts. The proposed techniques add design flexibilities for air core inductors that can lead to better electrical performance to the existing PCB and microfabrication techniques for high frequency power electronics converters. Specifically we will show examples of air core inductors that have circular cross sections, excellent copper coverage, and significant design flexibility. Moreover, we will demonstrate inductive structures that are difficult to manufacture using conventional laminar processes but yield relatively high  $Q$  numbers for a given inductance value. This paper also demonstrates one possible manufacturing process using online 3D printing and casting services to lower the economic hurdle for making inductors of complex geometries.

Furthermore, 3D printing combined with plating processes

such as sputtering or selective electroplating can yield complex passive structures capable of providing electrical isolation, or enhanced thermal performance.

Section II describes the design, modeling and fabrication process of the 3D printed air core inductors later used in a prototype power converter. In this section, we also discuss how the 3D models are imported into Finite Element Analysis (FEA) software to analyze and compare the electromagnetic field distribution, and predict electrical performance parameters. We also show some exemplary structures that highlight the type of structures that can be easily manufactured with 3D printing techniques. Section III discusses the quality factors measurements of the example inductors. Further details of the prototype and experimental results are shown in Section IV. Section V concludes the paper.

## II. 3D PRINTED AIR CORE INDUCTORS

Recent advances and increasing popularity in 3D printing has led to its application to almost every area of industry and every day life. Increased accessibility and performance has proven 3D printing technologies to be cost effective for prototyping components for research applications as well as consumer level products.

The popularity of 3D printing for rapid prototyping has resulted in a “makers community” that has led to dramatic reductions in system costs. Moreover, access to 3D printing technologies is becoming widespread through the advent of online businesses that provide 3D printing services in a variety of materials.

This work takes advantage of the accessibility and low cost of available 3D printing techniques and applies them to the manufacture of air core inductors suitable for high frequency switching power converters. Furthermore, a variety of techniques such as metalized plating, casting in metal, or direct metal printing allows for the creation of multi-function passive components with desirable electrical, mechanical, and thermal properties.

### A. 3D printing process

There are several types of 3D printing techniques, but the ones relevant to this paper are:

**Fused Deposition Modeling (FDM):** an additive manufacturing technique in which an extruded thermoplastic filament (commonly ABS or PLA) is passed through a heated nozzle, and the printing head deposits fused material selectively layer by layer in the X-Y coordinates of a heated plate to form the 3D model.

**Stereolithography (SLA):** an additive manufacturing technique in which a 3D object is printed out of thin layers of a “light” curable material. The laser cures points at the surface of a liquid resin which forms a layer of the 3D object, which is subsequently drawn out by a layer thickness and repeat the process.

**Selective laser sintering (SLS):** a high power laser or electron beam fuses small beads of material to form a layer of complex 3D objects. Material not sintered in a layer serves as support material for subsequent layers, allowing the inclusion

of overhang structures without the need of a different support material. Commercial system now use printing materials that include plastics polymers (nylon, polystyrene) and metals (steel, titanium, other alloys).

With currently available 3D printing technology, systems printing in thermoplastics and resins are far more affordable and available than systems that directly print in metal. So metalization of non-conductive models is essential for practical manufacturing of 3D printed circuit components. Specifically, lost wax casting is used for the realization of the 3D printed inductors described in this paper. It is expected that as interest in metal 3D printing increases, there will be more available options for direct manufacturing of some passive circuit components that may include the deposition of magnetic materials.

Fig. 2 shows the steps in the process for fabricating the 3D printed air core inductors described in this paper. The process begins with Fig. 2a which shows a 3D CAD model describing the geometry for the desired inductor. As 3D modeling opens the space to new possibilities, we encourage readers to explore online design communities such as MakerBot Thingiverse [37] for a glimpse of the creative geometries that are possible. In the second step, an SLA 3D printer is used to build a model of the inductor in a wax-based resin. The result is something similar to Fig. 2b, which is a similar design printed in plastic resin using a low cost stereolithography 3D printer from Formlabs.

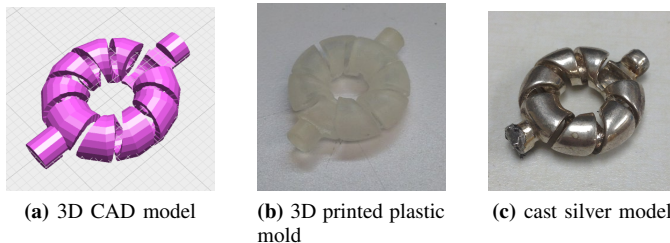


**Fig. 2:** Steps in the fabrication of a 3D inductor. (a) shows the OpenJSCAD model, (b) shows a translucent plastic model and (c) shows a sterling silver inductor. The 3D inductor has 10nH inductance and its dimensions are OD=18 mm, ID=6 mm, N=4. Also notice the rounded cross section.

The castable model is then used to make a plaster casting mold for use in lost wax casting techniques common to making jewelry. The inductor of Fig. 2c was cast in sterling silver. Companies such as i.materialise [38] and Shapeways [39] offer online 3D printing and casting services for jewelry items in soft metals like silver and gold. The casting of the inductors presented in this paper were done using their services. If the reader desires to look at the designs in more detail the models can be downloaded directly from i.materialise [40]. For the examples presented in this paper, we were somewhat limited by the manufacturing guidelines of i.materialise and Shapeways. Because of this, we were not able to optimize some component parameters such as supporting wall thickness and interwinding separation for our initial air core inductors. These limitations are not fundamental, but specific to the constraints of the low cost online manufacturers at this point in time. We will continue to explore the limits of casting based 3D implementations for the fabrication of circuit components.

Direct laser metal sintering can also be used to make some of the magnetic structures described here, but because of its high cost it was not considered here.

There are alternative ways of realizing the 3D air core inductors described in this paper. As mentioned in Section I, the method currently under investigation by the authors is to print the shape of the desired passive component in a non-metallic material (ABS, resin, etc) and use electro-deposition techniques similar to [29], [30] to plate the desired surfaces thus conferring the desired electrical characteristics to the structure.

This technique is very promising as it allows the plating of thin surfaces comparable to the skin depth of the ac current flowing through a given component at a designed switching frequency. This method may also offer additional benefits as it can help reduce the material cost and weight of the component. Moreover, it allows for sequential applications of conductive and insulating layers for the formation of primary and secondary windings of an isolated 1:1 air core transformer with good coupling.

We envision 3D printing of electronic components and structures that goes beyond the air core inductors described here. Specifically we are looking into the design of parts with the following attributes: *a*) combined 3D structures that incorporate parasitic capacitances and inductances as tuning parameters in the design of an air core high-frequency power converter; *b*) implementation of high frequency isolation transformers by selective electro-deposition; and *c*) the capacity to add structural texture to enhance cooling capabilities, thus turning component into a heatsink or an EMI shield.

### B. Software Toolchain

For this paper we not only investigated ways of modeling the 3D components for fabrication, but also ways to analyze the electrical and magnetic characteristics within the structures, so that they can be properly incorporated into a power electronics design.

The 3D CAD models for 3D printing such as in Fig. 2a were developed in OpenJSCAD [41], a script based online compiler and OpenSCAD [42], a script based 3D CAD modeler. Script-based CAD software offers more flexibility in our designs as it saves time compared to hand-drawn CAD software especially when multiple iterations are required for the optimization of component geometries. Once the design is finished, a 3D CAD model (usually in a .stl format) can be readily used for 3D printing.

In order to evaluate performance before manufacture we are also interested in creating an effective FEA model for simulation. In this work, we use an open source CAD software FreeCAD [43] to convert part of the inductor CAD model from a surface mesh to solid and then import it directly to the FEA software (COMSOL Multiphysics and ANSYS Maxwell were used in this paper). With part of the model already imported, geometry manipulation (union, difference, intersection, etc.) in the 3D FEA software allows the exact reconstruction of the geometry and thus the FEA analysis for the designed component. The simulated electromagnetic distribution is important

to predict component impedance, make EMI predictions of individual components, interconnected components, and eventually of the whole power converter. FEM simulation of the 3D printed passive components is important especially when using unconventional geometries. Besides COMSOL Multiphysics and ANSYS Maxwell, other 3D FEA programs (Elmer, etc) are under investigation to develop and finalize an accurate and efficient 3D FEA toolset that incurs little or no cost to the user.

With the FEA results and a few iterations, the 3D CAD model is finalized and sent to the 3D printer.

### C. Example Inductors and Initial Measurements

Several examples of air core inductors are manufactured using 3D printing and lost wax casting techniques to give an idea of the geometries that are possible to realize. Initial measurements including inductance and quality factor were performed to characterize the individual inductors. We have used two measurement methods: 1) Reflection method of Keysight (former Agilent) E5061B network analyzer with impedance measurement option. Test fixture includes Keysight 16201A and 16092A. Open, short, load and low loss capacitance calibrations were performed using Keysight calibration kit 16195B on the 16201A connector plane. After connecting 16092A to 16201A, open and short calibrations were performed on 16092A along with proper port extension to compensate the residual impedance and phase shift of the 16092A [44], [45]. Note that low loss capacitance calibration is important for phase calibration when measuring high quality factors (close to 90 degree phase) [46]. 2) Keysight E4980A precision LCR meter. The test fixture used here was the Keysight 16047E. Open and short calibrations were performed accordingly. Fig. 3 shows the impedance measurement range which has a lower accuracy limit than the reflection method of Keysight E5061B shown in Fig. 4. Thus, it can measure lower inductance values accurately than the E5061B. Moreover, it gives more accurate results for quality factor/dissipation factor (quality factor/dissipation factor accuracy is generally proportional to the impedance accuracy as stated in both [47] and [48] for high  $Q$  cases). Since E4980A only reaches 2 MHz, this method provides a comparison point at low frequencies.

For FEA simulations, we have used COMSOL and ANSYS Maxwell to obtain the inductances and quality factors at a range of frequency points. To demonstrate the quality factors the example inductors can achieve using pure copper, we simulated the inductors with 100% IACS conductivity, which is also close to the theoretical conductivity of sterling silver. Meanwhile, we also included the simulation results with actual measured electrical conductivity (37% IACS) of the cast material to compare with our measurement results. Discussions on the large discrepancies between the simulation with 100% IACS and actual measurement on quality factors are detailed in Section III.

1) *A toroid with a square cross section:* As an example of 3D printed inductors, Fig. 5a, 5b and 5c show the OpenSCAD CAD model, photo and simulated magnetic flux density plot of a square cross section toroid. The vertical connecting walls are solid compared to the PCB ones in [2], [3]. Moreover,

### Measurement accuracy

The impedance measurement calculation example below is the result of absolute measurement accuracy.

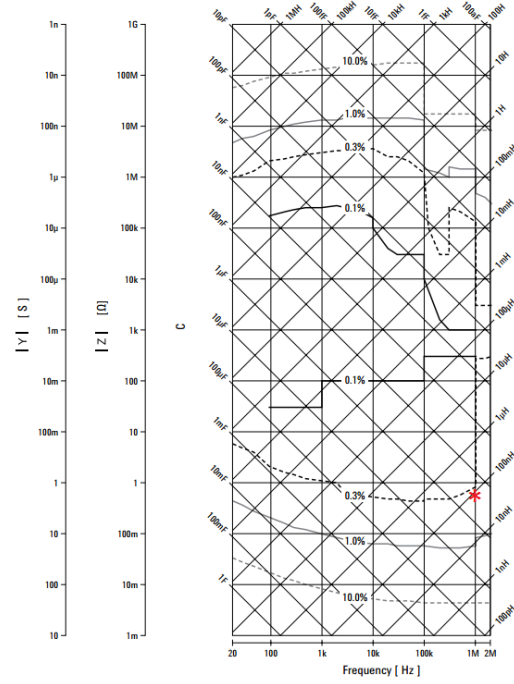


Figure 1. Impedance measurement accuracy (Test signal voltage = 1 Vrms, cable length=0 m, measurement time mode = MED)

Fig. 3: Measurement accuracy chart for E4980A LCR meter. The red star points out the measurement accuracy for a 100 nH inductor at 1 MHz and it is close to 0.3%.

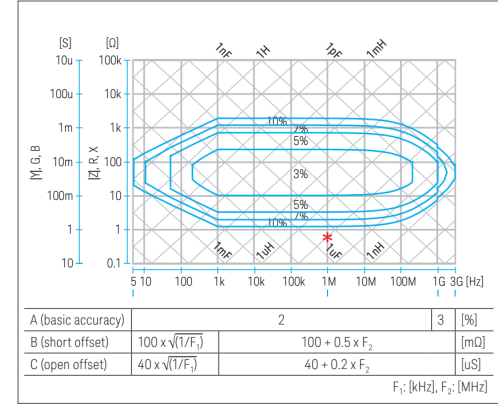
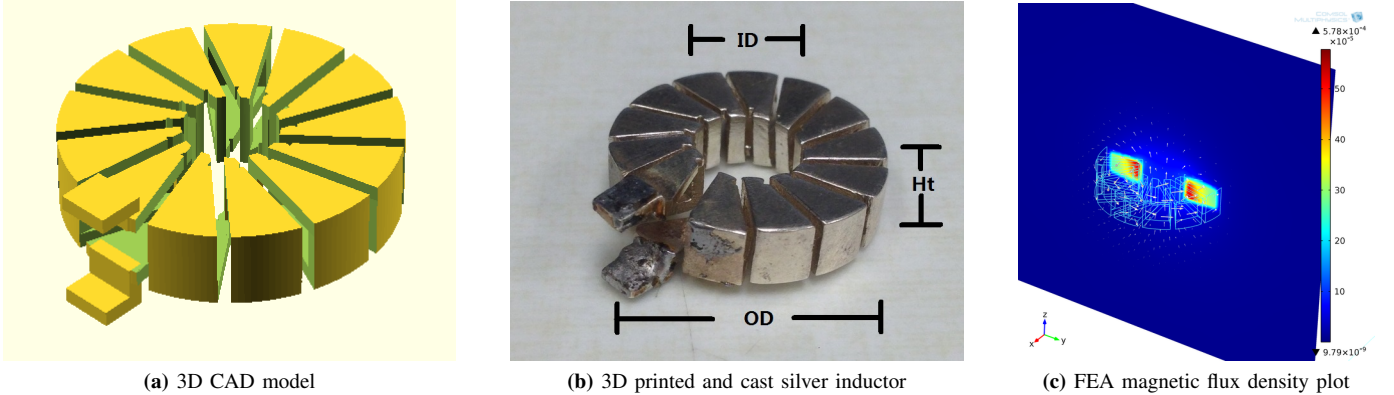


Figure 2. Impedance measurement accuracy (SPD), S-parameter part 1 reflection method.

Fig. 4: Measurement accuracy chart for reflection method of E5061B network analyzer with impedance measurement option. The red star points out the measurement accuracy for a 100 nH inductor at 1 MHz and it is outside of the 10% range.

ability to adjust the toroid height allows for designs with a better quality factor. Table I lists the measured and simulated inductances and quality factors  $Q$ . The quality factors and series resistances are also plotted in Fig. 6 and 7.

2) *A toroid with a circular cross section:* Fig. 8b shows a toroidal inductor with circular cross section. Fig. 8a shows the OpenJSCAD 3D CAD model. Magnetic field flux density was



**Fig. 5:** The toroid inductor with square cross section. The dimensions of the inductor: outer diameter 22mm, inner diameter 8mm, height 5mm, and 13 turns.

**TABLE I:** Simulated vs measured specification of the inductor in Fig. 5b. Simulation 1 and 2 show simulation results using 100% International Annealed Copper Standard (IACS) conductivity while simulation 3 uses the actual measured conductivity (37% IACS) of the cast material.

	L@27.12MHz nH	R@27.12MHz mΩ	Q@1 MHz	Q@2 MHz	Q@27.12 MHz	Q@54.24 MHz	Q@81.36 MHz
simulation1(COMSOL,100% IACS)	84.6	106.8	28.7	38.7	135	187	226
simulation2(Maxwell,100% IACS)	84.5	120.2	21.7	26.8	120	194	252
simulation3(Maxwell,37% IACS)	84.8	230	15	20	63	99	132
measurement w/ network analyzer	81	212	13	18.5	68	92.5	107
measurement w/ LCR meter	85@2MHz	54.8@2MHz	14	19.5	N/A	N/A	N/A

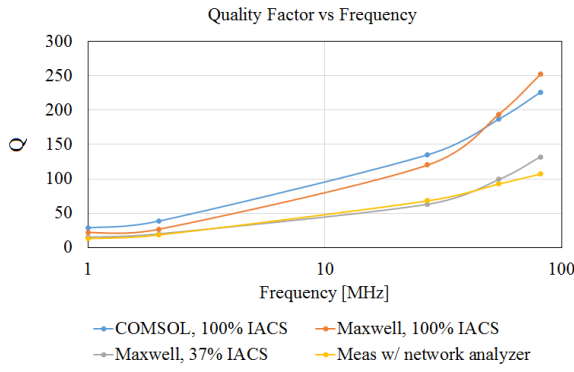


**Fig. 6:** Q measurement vs simulation of the inductor in Fig. 5b.

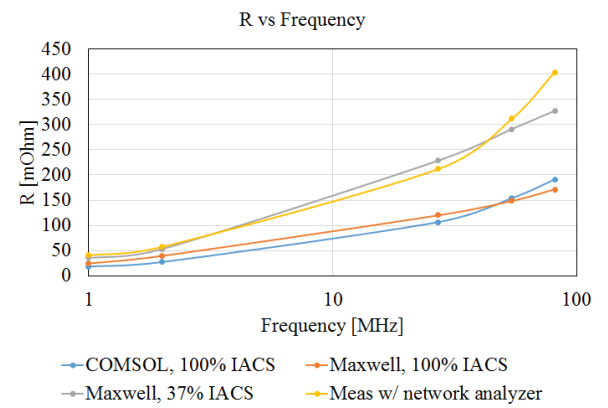


**Fig. 7:** Series resistance measurement vs simulation of the inductor in Fig. 5b.

simulated in COMSOL Multiphysics and shown in Fig. 8c. Table II lists the measured and simulated inductances and quality factors  $Q$ . The inductor in Fig. 8b was compared with its rectangular cross section counterpart in COMSOL Multiphysics. Table III details the characteristics of the two inductors for comparison. The quality factors and series resistances are also plotted in Fig. 9 and 10.

Machined air core inductors presented in the literature [13] make the toroid turns using vertical slits on the inductor walls. By using a 3D printer, we can print a scaffold that forms the inductor turns with a continuous spiral along the surface of the toroid. A circular cross section was chosen because it was simple to describe in 3D modeling software for 3D printing and offers improved performance over rectangular designs. Future work will involve optimization of the cross section further for minimum loss under geometric constraints as a circular cross section is still not the optimum shape. Using 3D

printing, it is straightforward to fabricate an air core inductor with an optimal cross section (like the one described in [13]) once an appropriate script for the CAD model is developed.

3) *A circular cross section toroid with parallel windings for axial flux cancellation.*: Work in [49] demonstrates the cancellation effect of the “one-turn” inductance caused by the circumferential current in an air core inductor. Specifically, paralleling two winding legs cancels the magnetic field caused by the circumferential current on each leg. However, the process used in [49] to manufacture the components resulted in air core inductors with rectangular cross section with a low vertical/width ratio. The geometry in Fig. 11a was designed to have a round cross section while achieving the same “one-turn” cancellation effect. The silver cast inductor is shown in Fig. 11b. Its magnetic field flux density plot was analyzed

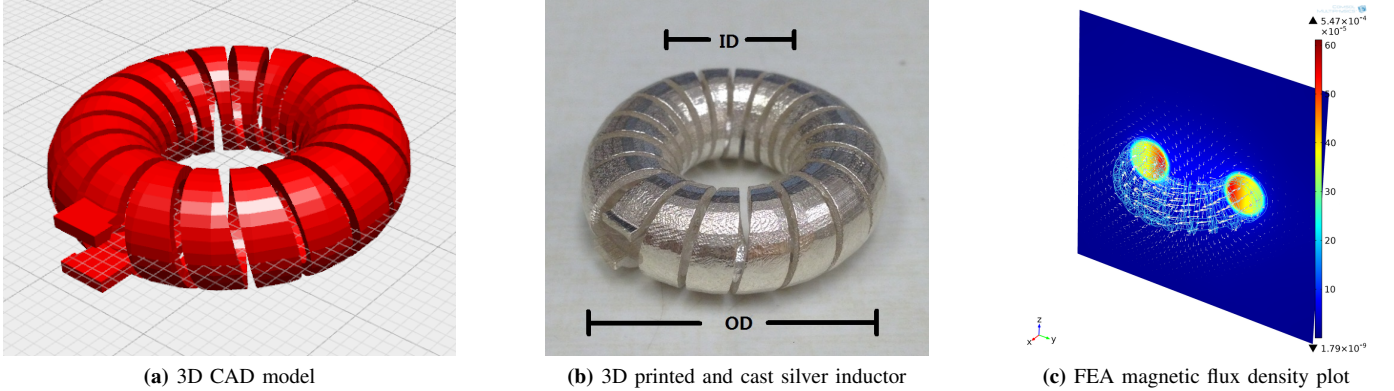


**Fig. 8:** The toroid inductor with circular cross section. The dimensions of the inductor: outer diameter 29mm, inner diameter 11mm, and 20 turns.

**TABLE II:** Simulated vs measured specification of the inductor in Fig. 8b. Simulation 1 and 2 show simulation results using 100% IACS conductivity while simulation 3 uses the actual measured conductivity (37% IACS) of the cast material.

	L@27.12MHz nH	R@27.12MHz mΩ	Q@1 MHz	Q@2 MHz	Q@27.12 MHz	Q@54.24 MHz	Q@81.36 MHz
simulation1(COMSOL,100% IACS)	341	246.2	50.5	68.4	236	313	355
simulation2(Maxwell,100% IACS)	340.3	230	46.8	64	252	326	430
simulation3(Maxwell,37% IACS)	346	480	29	41	123	185	250
measurement w/ network analyzer	345.5	460	22.5	35.5	125	175	200
measurement w/ LCR meter	348@2MHz	118@2MHz	27.6	37	N/A	N/A	N/A

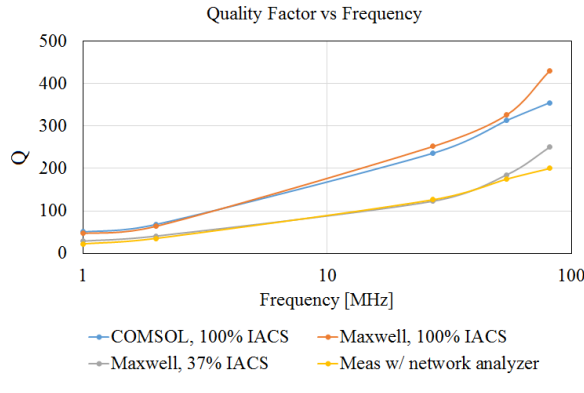


**Fig. 9:** Q measurement vs simulation of the inductor in Fig. 8b.

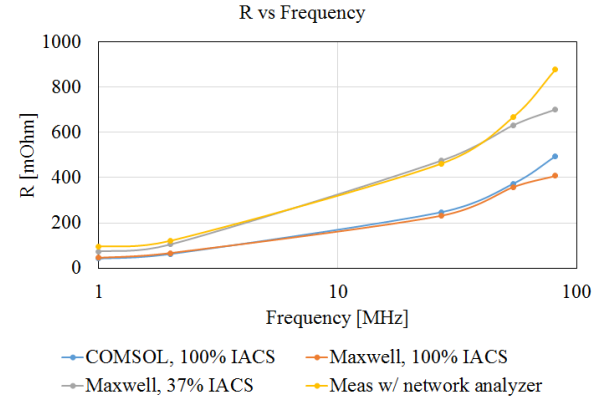


**Fig. 10:** Series resistance measurement vs simulation of the inductor in Fig. 8b.

**TABLE III:** COMSOL simulation comparison of inductor in Fig. 8b and its counterpart using 100% IACS.

	Round	Rectangular
OD(outer diameter)	29mm	29mm
ID(inner diameter)	11mm	12mm
h(height)	9mm	9mm
N(turns)	20	19
wall thickness	1mm	1mm
$L_{sim}$ @27.12MHz	341nH	365nH
Q@27.12MHz	236	217

in COMSOL Multiphysics and shown in Fig. 11c. Fig. 11c demonstrates that the magnetic field in  $z$  direction is much smaller relative to the whole field distribution compared with the normal toroid inductors in Fig. 5b and 8b. Table IV lists the measured and simulated inductances and quality factors  $Q$ .

4) *A toroid with a round cross section and four parallel windings:* As an example of the added flexibility, Fig. 12b shows an inductor design that can not be implemented in a planar process. Although 3D printing is an inherently laminar process, it creates a scaffold that when plated (or cast) result in a structure with features that current laminar PCB technology cannot achieve. The structure of Fig. 12b consists of four inductive legs that mutually cancel the “one turn” inductance in the respective toroidal planes. This reduces external fields in the structure, and prevents coupling with other components and may allow a close placement of components. This design favors applications where small inductances and high quality factors are required. Fig. 12a shows the 3D CAD model in OpenJSCAD. The magnetic flux density plot was obtained by using COMSOL Multiphysics and shown in Fig. 12c.

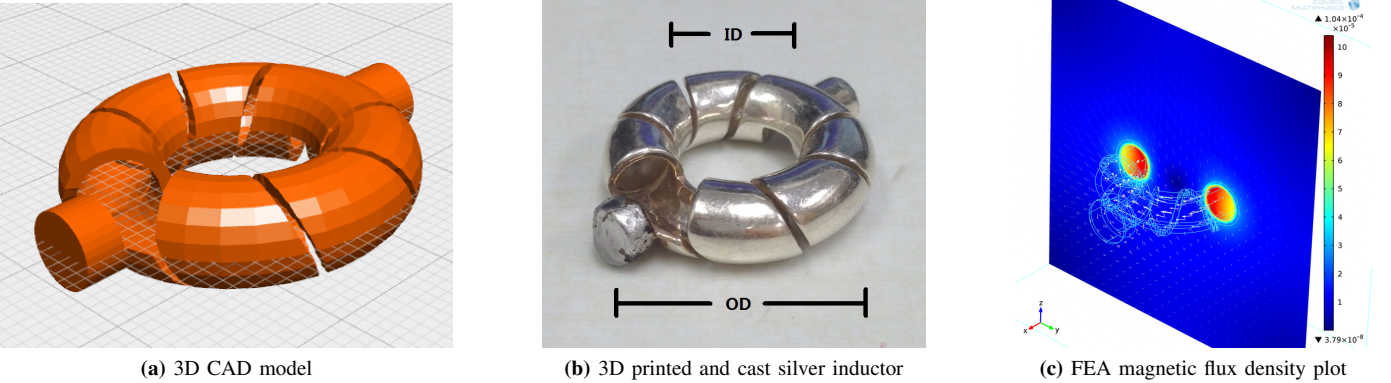


**Fig. 11:** The toroid inductor with circular cross section and two parallel windings. The dimensions of the inductor: outer diameter 28mm, inner diameter 12mm, and 4 turns for each winding.

**TABLE IV:** Simulated vs measured specification of the inductor in Fig. 11b. The electrical properties of this inductor put it outside the accuracy range of the E5061B used for measurement 1(Fig. 4) but still within the range of E4980A used for measurement 2 (Fig. 3). Simulation 1 and 2 show simulation results using 100% IACS conductivity while simulation 3 uses the actual measured conductivity (37% IACS) of the cast material.

	L@27.12MHz nH	R@2MHz mΩ	Q@1 MHz	Q@2 MHz	Q@27.12 MHz	Q@54.24 MHz	Q@81.36 MHz
simulation1(COMSOL,100% IACS)	24	3.6	60	83	293	411	501
simulation2(Maxwell,100% IACS)	20.4	3.1	65	82	297	406	555
simulation3(Maxwell,37% IACS)	20.8	4.4	38	58	No data	No data	No data
measurement w/ LCR meter	17.8@2MHz	3.9	40	58	N/A	N/A	N/A

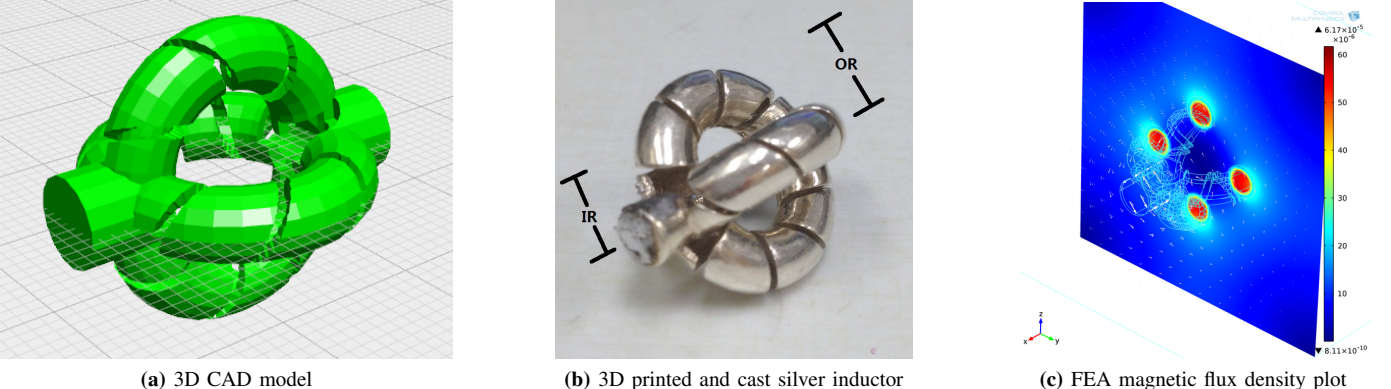


**Fig. 12:** The toroid inductor with circular cross section and four parallel windings. The dimensions of the inductor: outer diameter 21mm, inner diameter 10mm, and 4 turns for each winding.

Notice that there is very little magnetic field inside the empty volume of the inductor suggesting it may be possible to include similar inductive structures within, forming a nested magnetic structure to maximize the use of the volume. Table V lists the measured and simulated inductances and quality factors  $Q$ .

5) “One turn” inductance cancellation with oppositely wound series toroids: There are other ways to eliminate the “one turn” circumferential inductance. For example, Fig. 13b shows two toroidal inductors like the one of Fig. 8b connected in series. The two inductors have the same dimensions and number of turns but the windings go in opposite directions. By connecting one inductor with opposite windings on top of another, the circumferential current of the two inductors flow in opposite directions. Thus the magnetic field within the inner area of the inductor due to the circumferential current is

cancelled. Fig. 13a shows the 3D cad model in OpenJSCAD, while the magnetic flux density plot analyzed by COMSOL Multiphysics is plotted in Fig. 13c, which demonstrates the expected cancellation effect.

### III. DISCUSSION ON MEASUREMENTS OF QUALITY FACTORS

Upon characterizing the impedance of the 3D printed cast inductors it was found that while the simulated and measured inductance values matched very well, the quality factor of the measured inductors was on average 55 % of the simulation results using 100% IACS.

The discrepancy can come from three sources: simulation, measurement, and the inductors themselves. Additional designs of simpler geometries (e.g. 1 turn loops) whose induc-

**TABLE V:** Simulated vs measured specification of the inductor in Fig. 12b. The electrical properties of this inductor put it outside the accuracy range of the E5061B used for measurement 1 (Fig. 4) but still within the range of E4980A used for measurement 2 (Fig. 3). Simulation 1 shows simulation results using 100% IACS conductivity while simulation 3 uses the actual measured conductivity (37% IACS) of the cast material.

	L@27.12MHz nH	R@2MHz mΩ	Q@1 MHz	Q@2 MHz	Q@27.12 MHz	Q@54.24 MHz	Q@81.36 MHz
simulation1(COMSOL,100% IACS)	9.3	1.7	51	69.3	232	323	392
simulation3(Maxwell,37% IACS)	9.7	2.5	35	49	no data	no data	no data
measurement w/ LCR meter	9 @2MHz	2.5	30	46	N/A	N/A	N/A

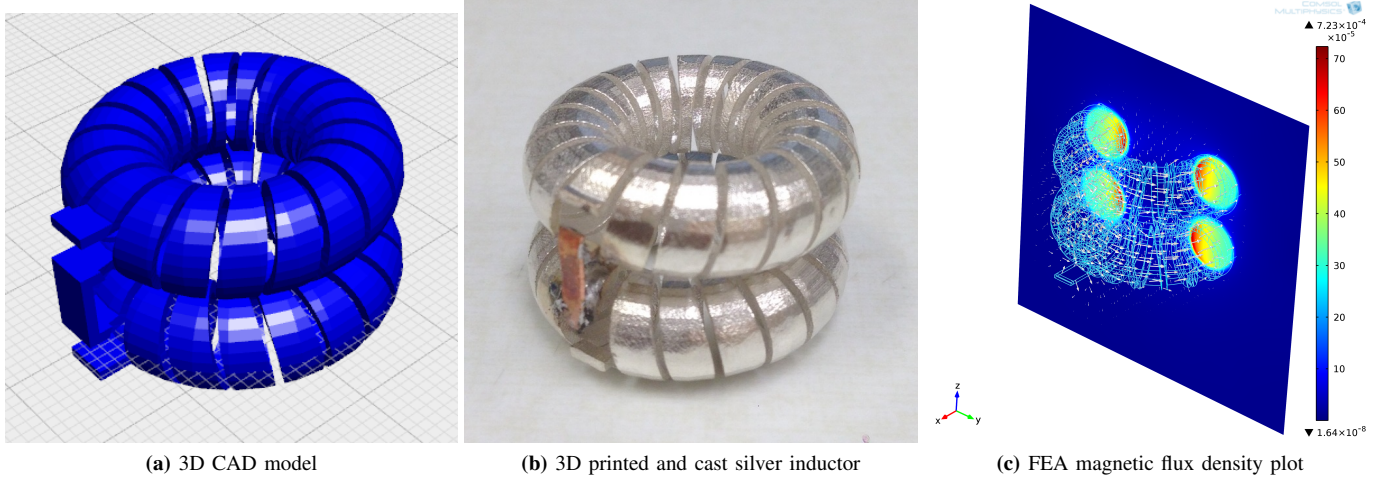


**Fig. 13:** Two toroid inductors in series with circular cross section and opposite winding directions. The dimensions of each inductor: outer diameter 29mm, inner diameter 11mm, and 20 turns.

tances, resistances and quality factors can be easily derived by hand calculation were created in attempts to resolve the quality factor discrepancy and corroborate the predictions of the FEA analysis.

We have designed three one turn loop inductors of different surface finish from two manufacturers as listed in table VI. Fig. 14 shows the 3D printed and cast silver part from the Shapeways. For comparison, we also implemented their copper counterparts with the same dimensions using magnet wire as shown in Fig. 14.

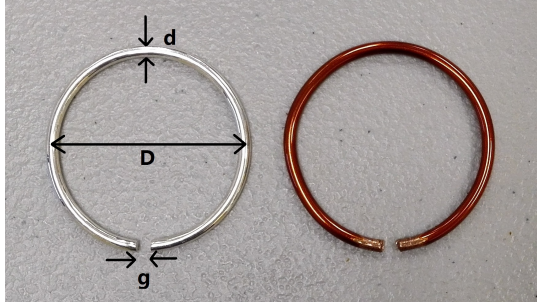


**Fig. 14:** One turn loop 3D printed and cast silver inductor and its copper counterpart.

Specifically, we a) measured the dc resistances of cast straight bars to obtain the conductivity of the sterling silver, b) simulated the inductances and quality factors of the one turns

and their copper counterparts and compare to calculation<sup>1</sup> in order to verify the simulation setup, c) measured the inductances and quality factors of the one turns and their copper counterparts in order to verify the measurement setup.

To obtain the conductivity of the cast material, we performed 4-wire dc resistance measurements of cast straight silver bars manufactured by Shapeways using an Agilent 34420A micro-ohm meter. We measured a conductivity of  $\approx 37\%$  IACS at dc for the cast silver, which leads to a  $Q$  of 61% of the predicted value ( $Q$  is approximately proportional to square root of conductivity). This closely agrees with the measured average  $Q$  values which are 55% of the predicted  $Q$  values as reported above. The additional measurement results of the dc resistances of single turn loops and the inductors of Section II are listed in Table VII and VIII.

To measure the inductance and quality factors of the one turns, we used the Keysight E4980A LCR meter due to its high accuracy for the targeted impedance range. In the interest of eliminating solder joints the ends of the one turn loops were clamped directly to a Keysight 16047E test fixture as shown in Fig. 15. The contact location results in slightly less measured inductance than calculation and simulation. Measurements of inductances and quality factors have been taken as an average of four measurements and standard deviations are provided. Further study will include investigation of better techniques for measuring high quality factors such as [51]–[53].

<sup>1</sup>The calculation of the inductance is obtained from equation 29 of [50]. The calculation of ac resistance is approximated as the deep skin depth case under the assumption that the current is uniformly distributed around the perimeter of the conductor to provide a baseline comparison of quality factor.

**TABLE VI:** Dimensions of the 3D printed and cast silver one turn inductors.

	Loop Diameter (D) [mm]	Wire Diameter (d) [mm]	Gap Length (g) [mm]	Surface finish	Manufacturer
One turn 1 (OT1)	30	2.05 (AWG12)	2	raw silver	Shapeways
One turn 2 (OT2)	30	2.05 (AWG12)	2	polished silver	Shapeways
One turn 3 (OT3)	30	2.05 (AWG12)	2	polished silver	i.materialise



**Fig. 15:** Connecting the one turn loop inductor to E4980A. The test fixture used is 16047E. Since the leads of the one turn loop are clipped directly, the contact location will result in a lower inductance than calculation and simulation.

Table IX lists the simulation, measurement and calculation results for the one turn inductors and their copper counterparts. It was found that the measured  $Q$  values of the silver cast one turns match the simulation and calculation results using the measured conductivity. Further, copper versions of the same geometries did not deviate significantly from the  $Q$  values predicted by the FEM simulations or hand calculations.

Thus, with the results above, we conclude the discrepancy between the measured and simulated (using 100% IACS) quality factors is due to the low conductivity (37% IACS) of the sterling silver from the online 3D printing and casting services. However, since we prefer surface copper plating to sterling silver casting for metalization, we do not think this is a major obstacle for the technology development but rather specific to the manufacturing process we chose for simplicity.

**TABLE VII:** Dc resistances of simulation and calculation for 3D printed and cast silver one turn inductors in Fig. 14 (listed as OT1 to OT3) and their copper counterpart (listed as OT1/2/3 Cu).

	$R_{DC,Meas}$ [mΩ]	$R_{DC,calc}$ [mΩ]
OT1	1.39	0.53
OT2	1.4	0.53
OT3	1.37	0.53
OT1/2/3 Cu	0.46	0.51

#### IV. EXPERIMENTS

The class  $\Phi_2$  inverter of Fig. 16 can reduce switch voltage stress by 30% – 40% below conventional class E derived

**TABLE VIII:** Dc resistances of simulation and measurement for 3D printed and cast silver inductors in Fig. 5 and Fig. 8

	$R_{DC,Meas}$ [mΩ]	$R_{DC,Sim}$ [mΩ]
L in Fig 5	5.8	2
L in Fig 8	11	4.33

**TABLE IX:** Simulation, measurement and comparison for 3D printed and cast silver one turn inductors (listed as OT1 to OT3) and their copper counterpart (listed as OT1/2/3 Cu). Measurement results are from the E4980A LCR meter. Simulation results are from ANSYS Maxwell. For the cast silver parts, the measured 37% IACS conductivity was used in simulation while the pure copper conductivity was for the copper counterpart.

	OT1	OT2	OT3	OT1/2/3 Cu
Meas. L [nH]	48.4	48.7	45	49.8
Std. Dev. [nH]	0.4	0.5	1	0.8
Sim. L [nH]	53.1	53.1	53.1	53.1
Calc. L [nH]	52.9	52.9	52.9	52.9
Meas. Q 1 MHz	44	53	48	78
Std. Dev.	1	2	4	2
Sim. Q 1 MHz	48	48	48	89
Calc. Q 1 MHz	50	50	50	84
Meas. Q 2 MHz	61	71	72	120
Std. Dev.	3	1	2	6
Sim. Q 2 MHz	65	65	65	126
Calc. Q 2 MHz	71	71	71	119

converters [54]–[59] and has been demonstrated to work efficiently at switching frequencies above 10 MHz. As described in [1],  $C_S$  blocks the dc component while  $L_S$  sets the ac power delivered to the load  $R_L$ . The remaining components

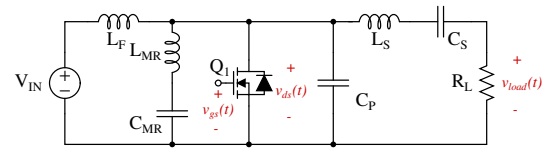


**Fig. 16:** Class  $\Phi_2$  Inverter

( $L_F$ ,  $L_{MR}$ ,  $C_{MR}$  and  $C_P$ ) form a resonant network having an impedance that shapes the MOSFET's off state voltage waveform to approximate a trapezoid of amplitude of about  $2V_{IN}$  [1], [60]. Design rules and methods to select component values are detailed in [1], [60].

To demonstrate an application of the 3D printed air-core inductors described here, a 70 W prototype  $\Phi_2$  inverter of Fig. 17 was designed and implemented. The assembly process associated with the converter involved the following steps: *a*) create 3D models of the desired inductor involved in the design, *b*) fabricate inductors and characterize impedance values and extract parasitics, *c*) connect resonant components to their respective nodes, and *d*) add semiconductor and filtering components.

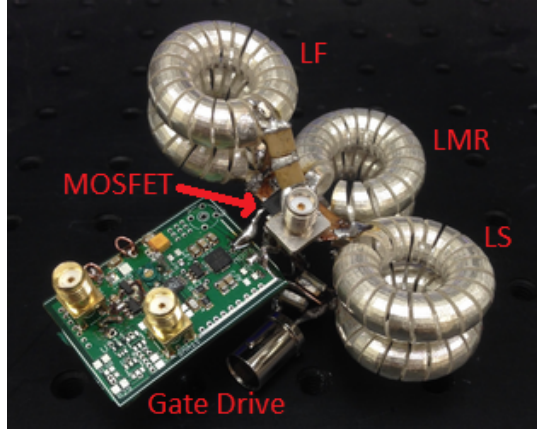


**Fig. 17:** Resonant inverter prototype photo

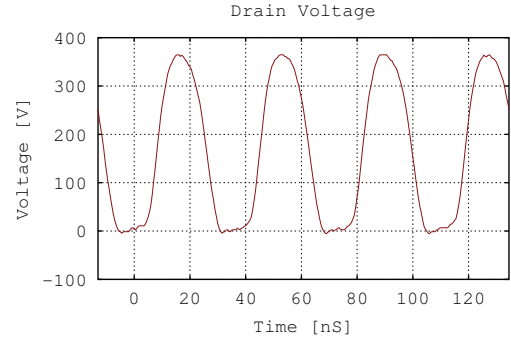


**Fig. 19:** MOSFET drain voltage waveform

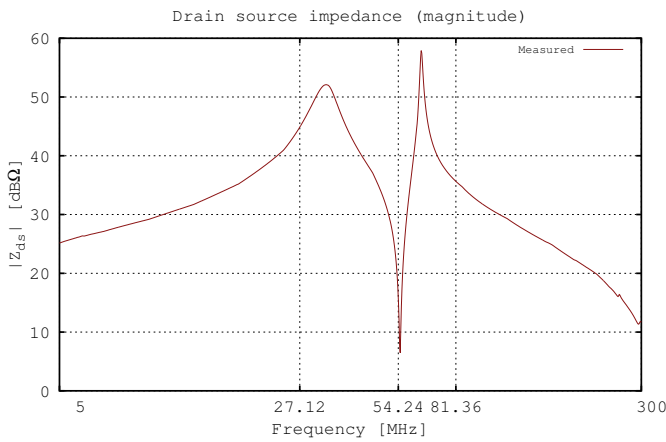


**Fig. 18:** Measured MOSFET drain to source impedance under bias condition  $V_{in}=170V$

For this initial proof of the concept, the 3D printed inductors were manufactured separately and soldered together. In the future, we expect to be able to print the combined structure with all the air core inductors and resonant capacitors in the circuit in one step, while being able to model the impedance of the structure and extract and/or absorb relevant parasitics into the design. This way, all the resonant passive components will be manufactured together and no further post processing or assembly will be necessary. A 27.12 MHz hard switched gate drive similar to the design in [2] was attached to the inverter and chosen for its simplicity. A self oscillating gate drive scheme is considered for future iterations, to create a fully 3D printed converter with all-in-one 3D printed passive components.

The MOSFET in the prototype is a silicon STMicroelectronics STD3NK50ZT4. For the inductors in the circuit, three identical inductors in Fig. 13b were used for simplicity as shown in Fig. 17. Thus, the inverter was not optimized for high efficiency but for ease of manufacturing, considering the turn-around times from the 3D printing companies. But the design was deemed appropriate as a proof of concept. Three

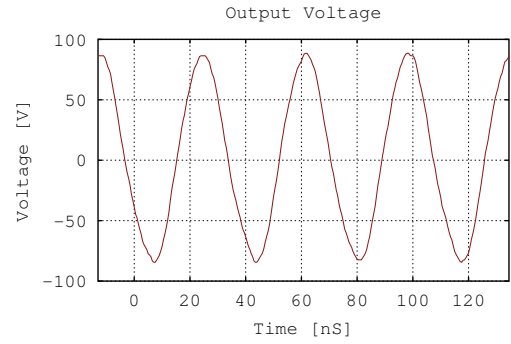


**Fig. 20:** Output voltage waveform

types of capacitors are used in the prototype inverter. The input capacitors consist of two series connected 250 V 1 nF X7R capacitors. The resonant capacitors,  $C_{MR}$  (12 pF) and  $C_P$  (30 pF) in Fig. 16 were at this point implemented with discrete ceramic capacitors. The larger dc blocking capacitor  $C_S$  is a 1.5 nF mica capacitor. The drain to source impedance is measured under the bias condition  $V_{in}=170V$  and shown in Fig. 18.

The 70 W prototype inverter operates at 27.12 MHz with an input voltage of 170 V. The output of the converter is connected to a  $50\ \Omega$  RF load resistor. Drain and output voltage waveforms of Fig. 19 and 20 are shown. The efficiency of the inverter reaches 80 %.

## V. CONCLUSION

This paper proposes the use of 3D printing and plating/casting techniques to add flexibility and functionality in the passive components design as they allow the manufacture of components with rounded edges and overhanging structures. In this paper, we present several examples of air core inductors designed using 3D printing and molding techniques demonstrating various geometries that are possible to realize. Moreover, we show that some of these designs can lead to improved electrical performance. The paper also describes the design tools used by the authors to design, fabricate, and characterize the electromagnetic performance of the air core

inductors. Toward this goal, we implemented a 70 W prototype 27.12 MHz resonant inverter that incorporates some of the 3D printed components developed for this work. Next steps include the implementation of optimal geometries, realization of other metalization techniques, and incorporation of thermal and mechanical characteristics to the FEM models. Further, we hope to implement the full structure of a high frequency power converter including passive components in FEM with the goal of printing the resultant structure.

## APPENDIX

### DESIGN CAPABILITIES FOR STERLING SILVER IN SHAPEWAYS

The capabilities of the manufacturing process used for the polished silver prototypes from Shapeways [61] are as follows:

- 1) Maximal bounding box:  $89 \times 89 \times 100$  mm
- 2) Minimal bounding box:  $2.4 \times 2.4 \times 0.6$  mm
- 3) Minimal supported wall thickness: 0.8 mm
- 4) Min unsupported wall thickness: 0.8 mm
- 5) Min supported wires: 0.8 mm
- 6) Min unsupported wires: 0.8 mm
- 7) Min embossed detail: 0.3 mm high and wide
- 8) Min engraved detail: 0.3 mm high and wide
- 9) Min escape holes: 0.4 mm diameter for one hole, 0.2 mm diameter for two or more holes
- 10) Clearance: 0.3 mm
- 11) No interlocking parts
- 12) Accuracy:  $\pm 0.125$  mm

The design guidelines for polished sterling silver 3D printing and casting process from i.materialise are similar and can be found in [62].

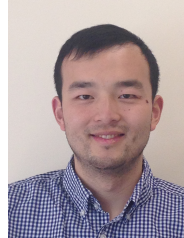
## ACKNOWLEDGMENT

The authors would like to thank Precourt Institute of Energy at Stanford University for the generous support of this work. The authors would also like to thank Mr. Lei Gu for the help provided throughout the editing of the manuscript.

## REFERENCES

- [1] J. M. Rivas, Y. Han, O. Leitermann, A. Sagneri, and D. J. Perreault, "A high-frequency resonant inverter topology with low voltage stress," in *Proc. IEEE Power Electronics Specialists Conf. PESC 2007*, 2007, pp. 2705–2717.
- [2] W. Liang, J. Glaser, and J. Rivas, "13.56 MHz high density dc-dc converter with PCB inductors," in *Applied Power Electronics Conference and Exposition (APEC), 2013 Twenty-Eighth Annual IEEE*, 2013, pp. 633–640.
- [3] L. Raymond, W. Liang, J. Choi, and J. Rivas, "27.12 MHz large voltage gain resonant converter with low voltage stress," in *Energy Conversion Congress and Exposition (ECCE), 2013 IEEE*, 2013, pp. 1814–1821.
- [4] X. Yu, M. Kim, F. Herrault, C.-H. Ji, J. Kim, and M. Allen, "Silicon-embedded 3d toroidal air-core inductor with through-wafer interconnect for on-chip integration," in *Proc. 2012 IEEE 25th International Conference on Micro Electro Mechanical Systems (MEMS)*, 2012, pp. 325–328.
- [5] J. Kim, F. Herrault, X. Yu, M. Kim, , and M. G. Allen, "Microfabrication of air core power inductors with metal-encapsulated polymer vias," *Journal of Micromechanics and Microengineering*, vol. 23, no. 3, pp. 1–7, 2013.
- [6] C.-H. Ji, F. Herrault, P. Hopper, P. Smeys, P. Johnson, and M. G. Allen, "Electroplated metal buried interconnect and through-wafer metal-filled via technology for high-power integrated electronics," *IEEE Trans. Adv. Packag.*, vol. 32, no. 3, pp. 695–702, 2009.
- [7] M. Araghchini, J. Chen, V. Doan-Nguyen, D. Harburg, D. Jin, J. Kim, M. S. Kim, S. Lim, B. Lu, D. Piedra, J. Qiu, J. Ranson, M. Sun, X. Yu, H. Yun, M. Allen, J. del Alamo, G. DesGroseilliers, F. Herrault, J. Lang, C. Levey, C. Murray, D. Otten, T. Palacios, D. Perreault, and C. Sullivan, "A technology overview of the powerchip development program," *IEEE Transactions on Power Electronics*, vol. 28, no. 9, pp. 4182 – 4201, 2013.
- [8] S. Rongxiang Wu ; Sin, J.K.O .; Hui, "A novel silicon-embedded coreless transformer for isolated DC-DC converter application," in *2011 IEEE 23rd International Symposium on Power Semiconductor Devices and ICs (ISPSD)*, 2011.
- [9] J. Rongxiang Wu ; Sin, "High-efficiency silicon-embedded coreless coupled inductors for power supply on chip applications," *IEEE Transactions on Power Electronics*, vol. 27, no. 11, pp. 4781–4787, 2012.
- [10] A. Fassler and C. Majidi, "Soft-matter capacitors and inductors for hyperelastic strain sensing and stretchable electronics," *Smart Materials and Structures*, vol. 22, no. 5, pp. 1–8, 2013.
- [11] N. Lazarus, C. Meyer, S. Bedair, H. Nochetto, and I. Kierzewski, "Multilayer liquid metal stretchable inductors," *Smart Materials and Structures*, vol. 23, no. 8, pp. 1–10, 2014.
- [12] M. Nigam and C. R. Sullivan, "Multi-layer folded high-frequency toroidal inductor windings," in *Proc. IEEE Applied Power Electronics Conference and Exposition, 2008. APEC 2008.*, 2008, pp. 682–688.
- [13] C. R. Sullivan, W. Li, S. Prabhakaran, and S. Lu, "Design and fabrication of low-loss toroidal air-core inductors," in *Proc. IEEE Power Electronics Specialists Conf. PESC 2007*, 2007, pp. 1754–1759.
- [14] M. Zolog, D. Pitica, and O. Pop, "Characterization of spiral planar inductors built on printed circuit boards," in *Electronics Technology, 30th International Spring Seminar on*, May 2007, pp. 308–313.
- [15] T. Andersen, C. Zingerli, F. Krismer, J. Kolar, and C. O'Mathuna, "Inductor optimization procedure for power supply in package and power supply on chip," in *Energy Conversion Congress and Exposition (ECCE), 2011 IEEE*, Sept 2011, pp. 1320–1327.
- [16] J. Vanek, I. Szendiuch, and J. Hladik, "Optimization of properties of planar spiral inductors," in *Electronics Technology, 30th International Spring Seminar on*, May 2007, pp. 235–238.
- [17] S. Orlandi, B. Allongue, G. Blanchot, S. Buso, F. Faccio, C. Fuentes, M. Kayal, S. Michelis, and G. Spiazz, "Optimization of shielded PCB air-core toroids for high efficiency dc-dc converters," *IEEE Transactions on Power Electronics*, vol. 26, pp. 1837–1846, 2011.
- [18] R. Kamali-Sarvestani and J. Williams, "Fabrication of high quality factor rf-resonator using embedded inductor and via capacitor," in *IECON 2010 - 36th Annual Conference on IEEE Industrial Electronics Society*, Nov 2010, pp. 2283–2287.
- [19] S. Tang, S. Hui, and H.-H. Chung, "Coreless printed circuit board (PCB) transformers with multiple secondary windings for complementary gate drive circuits," *IEEE Transactions on Power Electronics*, vol. 14, no. 3, pp. 431–437, 1999.
- [20] H. Schneider, T. Andersen, A. Knott, and M. Andersen, "Hybrid winding concept for toroids," in *Proc. 2013 IEEE ECCE Asia Downunder (ECCE Asia)*, 2013, pp. 936–940.
- [21] ———, "Optimizing DC-resistance of a foil wounded toroidal inductor combining MATLAB and COMSOL," in *Proc. AFRICON, 2013*, 2013, pp. 1 – 5.
- [22] M. Nigam and C. Sullivan, "Multi-layer folded high-frequency toroidal inductor windings," in *Applied Power Electronics Conference and Exposition, 2008. APEC 2008. Twenty-Third Annual IEEE*, Feb 2008, pp. 682–688.
- [23] C. Meyer, S. Bedair, B. Morgan, and D. Arnold, "A micromachined wiring board with integrated microinductor for chip-scale power conversion," *Power Electronics, IEEE Transactions on*, vol. 29, no. 11, pp. 6052–6063, Nov 2014.
- [24] J. Kim, F. Herrault, X. Yu, and M. Allen, "Microfabrication of air-core toroidal inductor with very high aspect ratio metal-encapsulated polymer vias," in *Proc. PowerMEMS, 2012*, pp. 30 – 33.
- [25] J. Zou, C. Liu, D. Trainor, J. Chen, J. Schutt-Aine, and P. Chapman, "Development of three-dimensional inductors using plastic deformation magnetic assembly (PDMA)," *IEEE Transactions on Microwave Theory and Techniques*, vol. 51, pp. 1067–1075, 2003.
- [26] C. Chua, D. K. Fork, K. van Schuylenbergh, and J.-P. Lu, "Out-of-plane high-Q inductors on low-resistance silicon," *Journal of Microelectromechanical Systems*, vol. 12, no. 6, pp. 989–995, 2003.
- [27] N. Chomnawang, J.-B. Lee, and W. A. Davis, "Surface micromachined arch-shape on-chip 3-D solenoid inductors for high-frequency applications," *Journal of Micro/Nanolithography, MEMS, and MOEMS*, vol. 2, no. 4, pp. 275–281, 2003.

- [28] N. Chomnawang, "Three-dimensional micromachined on-chip inductors for high frequency applications," Ph.D. dissertation, Louisiana State University, 2002.
- [29] Y.-K. Yoon, J.-W. Park, and M. Allen, "Polymer-core conductor approaches for rf mems," *Microelectromechanical Systems, Journal of*, vol. 14, no. 5, pp. 886–894, Oct 2005.
- [30] Y.-K. Yoon, J.-H. Park, and M. Allen, "Multidirectional uv lithography for complex 3-d mems structures," *Microelectromechanical Systems, Journal of*, vol. 15, no. 5, pp. 1121–1130, Oct 2006.
- [31] A. Borysenko and K. Vanhille, "300 ghz microfabricated waveguide slotted arrays," in *Infrared, Millimeter, and Terahertz waves (IRMMW-THz), 2014 39th International Conference on*, Sept 2014, pp. 1–2.
- [32] J. Oliver, H. Kazemi, J.-M. Rollin, D. Sherrer, S. Huettner, and S. Raman, "Compact, low-loss, micromachined rectangular coaxial millimeter-wave power combining networks," in *Microwave Symposium Digest (IMS), 2013 IEEE MTT-S International*, June 2013, pp. 1–4.
- [33] W. Fathelbab, "Generalised parallel-coupled line and interdigital filters with unusually broad upper stop bandwidth: synthesis and design in homogeneous media," *Microwaves, Antennas Propagation, IET*, vol. 7, no. 5, pp. 306–324, April 2013.
- [34] J. Reid, J. Oliver, K. Vanhille, and D. Sherrer, "Three dimensional metal micromachining: A disruptive technology for millimeter-wave filters," in *Silicon Monolithic Integrated Circuits in RF Systems (SiRF), 2012 IEEE 12th Topical Meeting on*, Jan 2012, pp. 17–20.
- [35] Z. Popovic, "Micro-coaxial micro-fabricated feeds for phased array antennas," in *Phased Array Systems and Technology (ARRAY), 2010 IEEE International Symposium on*, Oct 2010, pp. 1–10.
- [36] D. Sherrer, J. ROLLIN, K. Vanhille, M. Oliver, and S. Huettner, "Three-dimensional microstructures," Aug. 7 2014, uS Patent App. 14/253,061. [Online]. Available: <https://www.google.com/patents/US20140218131>
- [37] MakerBot Thingiverse. Online 3D Printing Design Community. [Online]. Available: <http://www.thingiverse.com/>
- [38] i.materialise. Online 3D printing service. [Online]. Available: <http://i.materialise.com/>
- [39] Shapeways. Online 3D printing service. [Online]. Available: <http://www.shapeways.com>
- [40] SUPER Lab i.materialise Shop. Online 3D Model Gallery. [Online]. Available: <http://i.materialise.com/shop/designer/SUPER-Lab>
- [41] Open JSCAD. Computer Software. [Online]. Available: <http://openjscad.org/>
- [42] Open SCAD. Computer Software. [Online]. Available: <http://openscad.org/>
- [43] FreeCAD. Computer Software. [Online]. Available: <http://www.freecadweb.org>
- [44] Impedance Measurement With E5061B LF-RF Network Analyzer Slides. Keysight Technologies. [Online]. Available: <http://literature.cdn.keysight.com/litweb/pdf/5991-0213EN.pdf>, 2011
- [45] E5061B Network Analyzer PDF Help (For Firmware Rev. A.02.0x). Keysight Technologies. [Online]. Available: <http://www.keysight.com/main/editorial.jspx?cc=US&lc=eng&ckey=1814709&nid=33831.912674.00&id=1814709,2011>
- [46] How To Accurately Evaluate Low ESR/High Q RF Chip Devices (AN 1369-6). Keysight Technologies. [Online]. Available: <http://www.keysight.com/main/techSupport.jspx?cc=US&lc=eng&nid=33831.536880679.08&pid=1000003705%3Aepsg%3Apro&pageMode=OV,2004>
- [47] Keysight E4980A/L Precision LCR Meter. Keysight Technologies. [Online]. Available: <http://cp.literature.agilent.com/litweb/pdf/5989-4435EN.pdf>
- [48] Keysight E5061B-3L5 LF-RF Network Analyzer with Option 005 Impedance Analysis Function. Keysight Technologies. [Online]. Available: <http://literature.cdn.keysight.com/litweb/pdf/5990-7033EN.pdf>
- [49] J. Qiu, A. Hanson, and C. Sullivan, "Design of toroidal inductors with multiple parallel foil windings," in *Proc. IEEE 14th Workshop on Control and Modeling for Power Electronics (COMPEL)*, 2013, 2013, pp. 1–6.
- [50] F. Terman, *Radio Engineers' Handbook*, first edition, tenth impression ed. New York and London: McGraw-Hill, 1943.
- [51] K. O, "Estimation methods for quality factors of inductors fabricated in silicon integrated circuit process technologies," *Solid-State Circuits, IEEE Journal of*, vol. 33, no. 8, pp. 1249–1252, Aug 1998.
- [52] S. Prabhakaran and C. Sullivan, "Impedance-analyzer measurements of high-frequency power passives: techniques for high power and low impedance," in *Industry Applications Conference, 2002. 37th IAS Annual Meeting. Conference Record of the*, vol. 2, Oct 2002, pp. 1360–1367 vol.2.
- [53] P. J. Petersan and S. Anlage, "Measurement of resonant frequency and quality factor of microwave resonators: Comparison of methods," *Journal of Applied Physics*, vol. 84, no. 6, pp. 3392–3402, 1998.
- [54] N. Sokal and A. Sokal, "Class E-a new class of high-efficiency tuned single-ended switching power amplifiers," *IEEE Journal of Solid-State Circuits*, vol. 10, pp. 168–176, 1975.
- [55] R. Redl and N. Sokal, "A 14 MHz 100 Watt class E resonant converter:principles, designconsiderations, and measured performance," in *17th Annual IEEE Power Electronics Specialists Conference Proceedings*, 1986.
- [56] R. Redl, B. Molnar, and N. Sokal, "Class E resonant regulated dc/dc power converters: analysis of operations and experimental results at 1.5 MHz," *IEEE Transactions on Power Electronics*, vol. PE-1 no.2, pp. 111–120, 1986.
- [57] R. Redl and N. Sokal, "A new class-E dc/dc converter family with reduced parts count: derivation, topologies and design considerations," in *1989 Technical Papers of the Fourth International High Frequency Power Conference*, 1989.
- [58] J. Jozwik and M. Kazimierczuk, "Analysis and design of class E<sup>2</sup> dc/dc converter," *IEEE Transactions on Industrial Electronics*, vol. 37, pp. 173–183, 1990.
- [59] H. Koizumi, M. Iwadare, and S. Mori, "Class E<sup>2</sup> dc-dc converter with second harmonic resonant class E inverter and class E rectifier," in *3rd Annual Applied Power Electronics Conference Proceedings*, 1994.
- [60] J. M. Rivas, O. Leitermann, Y. Han, and D. J. Perreault, "A very high frequency dc–dc converter based on a class Φ<sub>2</sub> resonant inverter," vol. 26, no. 10, pp. 2980–2992, 2011.
- [61] Shapeways printing service silver material. Online 3D Printing and Casting service. [Online]. Available: <http://www.shapeways.com/materials/silver>
- [62] i.materialize printing service silver material. Online 3D Printing and Casting service. [Online]. Available: <http://i.materialise.com/materials/silver>



**Wei Liang** (S'12) received the B.Eng. degree from Northwestern Polytechnical University, Xian, China, and the M.S.E. degree from the University of Michigan, Ann Arbor, MI, USA, in 2011 and 2013, respectively. He is currently working toward the Ph.D. degree at the Stanford University Power Electronics Research Laboratory, Stanford University, Stanford, CA, USA. His research interests include high frequency power electronics and the air-core passive components design for VHF power conversion.



applications.



**Juan Rivas** (S'01-M'06) was born in Mexico City, Mexico. He received the B.A.Sc. degree from the Monterrey Institute of Technology, Monterrey, Mexico, in 1998, and the S.M. and Sc.D. degrees from the Laboratory of Electromagnetic and Electronic Systems, Massachusetts Institute of Technology, Cambridge, MA, USA, in 2003 and 2006, respectively.

From 2007 to 2011, he was a Power Electronics Engineer in the high-frequency power electronics group at the General Electric Global Research Center, Niskayuna NY, USA. From 2011 to 2013, he was an Assistant Professor at the University of Michigan, Ann Arbor, MI, USA. In 2014, he joined Stanford University, Stanford, CA, USA, as an Assistant Professor in the Electrical Engineering Department. His research interests include power electronics, RF power amplifiers, resonant converters, soft switching topologies, and the design of air-core passive components for VHF power conversion.